CO self-sustained catalytic combustion over morphological inverse model CeO₂/Cu₂O catalysts exposing (1 0 0), (1 1 1) and (1 1 0) planes

Zihao Teng [a], Xiaokun Yi [a], Chenhang Zhang [a,b], Chi He [c], Yulong Yang [a], Qinglan Hao [a], Baojuan Dou [a,*], Feng Bin [b,d,**]

[a] Tianjin University of Science & Technology, Tianjin 300457, PR China
[b] State Key Laboratory of High-Temperature Gas Dynamics, Institute of Mechanics, Chinese Academy of Sciences, Beijing 100190, PR China
[c] State Key Laboratory of Multiphase Flow in Power Engineering, Xi'an Jiaotong University, Xi'an 710049, PR China
[d] School of Engineering Science, University of Chinese Academy of Sciences, Beijing 100049, PR China

ARTICLE INFO

ABSTRACT

CO self-sustaining catalytic combustion tends to be one of potential means to achieve efficient conversion of off-gases from steelmaking. Building model catalysts to investigate the reaction process academically is essential to design optimized catalysts and Cu₂O exposing (1 0 0), (1 1 1) and (1 1 0) planes are excellent materials. Herein, morphological CeO₂/Cu₂O inverse model catalysts were synthesized to reveal the synergistic effect and reaction mechanism. It is demonstrated that the ignition temperature is lowered on the interface by synergistic effect, which dominates the ignition, while the combustion after ignition is controlled by Cu₂O planes providing abundant lattice oxygen to react with CO. Additionally, exposure of different planes plays a significant role in the reaction since O-termination on (1 0 0) inhibits the interaction, whereas Cu-termination on (1 1 0) surface structure and coordinately unsaturated Cu⁺ on open (1 1 1) surface respectively contribute to their superior catalytic performance.

1. Introduction

Off-gases emitted by basic oxygen furnace (BOF) in steel-making industry contain an appreciable amount of CO (<35%) and O₂ (>2%). Potential risk of explosion prohibits the mixture from direct reusage or discharge. In this case, the off-gases are generally combusted by methanol before released into the atmosphere and they occupy at least 20% of the total by-product gases. The annual consumption of CH₄ for off-gases causes not only an extravagant waste of energy but also excessive emission of CO₂ or even NOₓ. The CO self-sustained catalytic combustion is considered as a practical alternative to methanol combustion and it can be described as an energy-saved and environmental-friendly way to treat the off-gases, which can make full use of the heat produced by the exothermic reaction (2CO+O₂→CO₂ +12.64 MJ/Nm³). Once the catalytic reactor reaches the ignition temperature, a thermochemical runaway will result in a sharp jump in reaction temperature, followed by a sudden transition from intrinsic reaction kinetics step to self-sustained combustion step. The reaction can then keep going on without external

heating source as long as there is adequate supply of off-gases. The extra heat may be expected to be applied in other field such as thermal power generation.

All in all, the CO self-sustained catalytic combustion has noticeable potential for exploration but investigation on self-sustained combustion of high CO concentration is relatively scarce, since a majority of discoveries were carried out under low CO concentration (<1%), which generally present reaction behaviour different from those under high concentration. Current study on CO self-sustained catalytic combustion mostly focuses on the precise reaction mechanism and structure-effect correlation of original catalysts. A thorough comprehension of the two fundamental but vital aspects will be conducive to provide more basis for this method to be practical.

Owing to the outstanding catalytic activity and convenient accessibility, copper oxide catalysts have been widely studied as components in some important catalytic systems, such as preferential CO oxidation (CO-PROX), water-gas-shift (WGS) and NO reduction [1–3]. Especially, research about copper-supported ceria catalysts has made great progress

---

* Corresponding author.
** Corresponding author at: State Key Laboratory of High-Temperature Gas Dynamics, Institute of Mechanics, Chinese Academy of Sciences, Beijing 100190, PR China.
E-mail addresses: bjdou@tust.edu.cn (B. Dou), binfeng@imech.ac.cn (F. Bin).

with efficiency expected to be comparable to noble metal catalysts [4]. Our group have also found in previous work that CuCeZr/CuCe catalysts can perform promisingly in CO self-sustained catalytic combustion [5, 6]. During the investigation, the synergistic effect between copper and cerium was observed and it was found to take the main responsibility for the excellent catalytic activity [7]. It is generally acknowledged that thanks to the electron distribution of Ce^{4+} 4 f^0, CeO_2 possesses a particular property of transformation to the non-stoichiometric form of CeO_{2-x}, with the increased content of Ce^{3+} and oxygen vacancies, which makes great contribution to its compelling capacity of electron transfer and oxygen storage-release [8,9]. It is also reported that when other materials, such as copper oxides, are incorporated by CeO_2, the interaction between copper and cerium will lead to the synergistic effect on the Cu-Ce interface [10]. A redox equilibrium of $Ce^{4+}+Cu^+\leftrightarrow Ce^{3+}+Cu^{2+}$ is consequently formed and oxygen vacancies are concurrently produced to maintain the charge neutrality [11].

Nevertheless, the synergistic effect has not been demonstrated throughout in our early work since the specific interface where the interaction happens is difficult to locate due to the irregular shape of CuO, which causes problems to the observation and investigation focused on the interface. Recently, more and more studies about morphological catalysts have been published. Kinds of morphological catalysts have been successfully prepared and a plenty of catalysts with specific shapes were reported to expose sole crystal plane, such as CeO_2 (1 1 1) or Cu (1 1 1) [12–15], which provides accessibility for researchers to control the reaction interface and experiments targeted at the interface can be conducted. Hence, these researches have triggered awareness on the development of the morphological Cu_2O since Cu_2O with regular shapes can also expose one crystal plane, such as (1 1 1), (1 1 0) or (1 0 0), and the exposed crystal planes have been proved in one of our research projects to be critical in leading to different catalytic performance during the combustion [16]. Besides, our previous study about CuO and CuO-CeO$_2$ catalysts has found that the ignition temperature can be apparently decreased on the CuO-CeO$_2$ interface and however the CuO catalyst is capable of providing abundant oxygen and adsorption sites for the non-flame combustion with higher zone temperature during the self-sustained phase [7]. Due to the demand for rapid ignition under low temperature and stable self-sustained combustion with high efficiency, the idea has occurred to us that CeO_2 can be inversely loaded onto morphological Cu_2O to prepare catalysts which are known as the inverse model catalysts [17]. Inverse model catalysts have been proved to be feasible in exploring the reaction on the interface with more surface defect and dense functional sites. For example, Jia [18] et al. evaluated the catalytic activity of conventional model CuO/CeO$_2$ catalyst and inverse CeO$_2$/CuO catalyst by controlling the same size of loaded CuO and CeO$_2$ particles. It was concluded that both kinds of catalysts shared highly similar activity, indicating the interface of Cu-Ce as the active site for CO oxidation. The same approach has also been applied in other materials, which usually brings extraordinary catalytic performance to the catalysts. Li et al. [19] prepared inverse ZnO/Cu$_2$O catalysts via deposition method, which were used for Rochow reaction. It was shown that the deposition of ZnO effectively facilitated the catalytic activity of Cu$_2$O by generating more P-N junctions. Jian et al. [20] synthesized Au core-CeO$_2$ shell sub-microspheres, which were applied to the catalytic oxidation of CO. Compared to conventional supported Au/CeO$_2$ catalysts, the full conversion temperature of inverse Au@CeO$_2$ catalysts was significantly promoted from 300 °C to 150 °C. Rodriguez et al. [21] investigated the WGS reaction over CeO$_x$/Cu(1 1 1) inverse catalysts, finding that the inverse catalysts performed better than conventional Cu/CeO$_2$ catalysts due to the Cu-Ce interaction that accelerated the dissociation of water and chemisorption of CO. Hornes et al. [22] reported that approximately 100% selectivity towards CO could be reached in CO-PROX reaction over the inverse CeO$_2$/Cu catalysts because more reduced CuO$_x$ species were produced in this system, which acted as the main active sites for CO oxidation. These results inspired us that the inverse model CeO$_2$-Cu$_2$O system can be a worthwhile strategy

for figuring out the synergistic effect of copper and cerium as well as the reaction mechanism.

Herein, we reported the performance of inverse CeCu$_2$ catalysts with various morphology (cubes, octahedra and rhombic dodecahedra) in CO self-sustained catalytic combustion. It is found that CO self-sustained combustion can be favorably achieved over the catalysts and the ignition temperature has been declined owing to the synergistic effect on the interface between Cu$_2$O and CeO$_2$. Cu$^+$ is confirmed to be the active sites for CO adsorption and Cu$_2$O provides enough lattice oxygen for the reaction and in this situation Mars-van Krevelen (M-K) mechanism is dominant. Moreover, the catalytic activity and synergistic effect are closely associated with the crystal planes exposed in the order of Cu$_2$O (1 1 1) > (1 1 0) > (1 0 0). These results are expected to not only offer readers with better appreciation of the essence of the synergistic effect as well as the reaction mechanism, but also provide feasible methods of designing optimized catalysts.

2. Experimental

2.1. Preparation

Morphological Cu$_2$O nanocrystals were prepared by solution-phase synthesis method, which were labeled as Cu$_2$O-6 (cubic Cu$_2$O), Cu$_2$O-8 (octahedral Cu$_2$O) and Cu$_2$O-12 (rhombic dodecahedral Cu$_2$O), respectively. After the removal of capping ligands, the inverse CeO$_2$/Cu$_2$O catalysts were synthesized by impregnation method, which were correspondingly denoted as CeCu$_2$-6, CeCu$_2$-8 and CeCu$_2$-12.

2.1.1. Morphological Cu$_2$O nanocrystals

Cu$_2$O-6 and Cu$_2$O-8: 1 L of 0.01 mol/L CuCl$_2$·2H$_2$O solution (with 88.8 g polyvinylpyrrolidone for Cu$_2$O-8) was poured into a three-neck flask and kept in water bath under 55 °C with magnetic stirring for 30 min. Subsequently, 100 mL of NaOH solution (2 mol/L) was added into the container and the mixture was stirred for another 30 min. After that, 300 mL of glucose solution (0.104 g/mL) was used as reductant to reduce Cu^{2+} to Cu$^+$ and brick red Cu$_2$O nanocrystals could be obtained after 5-hour reaction. The product was washed and centrifuged with deionized (DI) water and ethanol for several times, finally dried in vacuum at 60 °C for 12 h.

Cu$_2$O-12: 500 mL of CuCl$_2$·2 H$_2$O solution (0.025 mol/L) was first poured into a three-neck flask. A mixture of 50 mL oleic acid (OA) and 250 mL ethanol was added into the solution, which was then kept in oil bath under 100 °C. After vigorous stirring for 30 min, the liquid was blended with 125 mL of NaOH solution (0.8 mol/L), followed by another 30-minute stirring. Subsequently, 375 mL of glucose solution (0.104 g/mL) was added as reductant and brick red Cu$_2$O nanocrystals could be obtained after one-hour reaction. The product was washed and centrifuged with DI water and ethanol for several times, finally dried in vacuum at 60 °C for 12 h.

2.1.2. Removal of surface ligands

The residual surface ligands (PVP or OA) on the catalysts will cause inhibition to the catalytic activity, thus they were removed by a redox process in a mixed stream of C$_3$H$_6$, O$_2$ and N$_2$. As-synthesized Cu$_2$O nanocrystals were exposed in the flow of 25 mL/min with a volume ratio of C$_3$H$_6$: O$_2$: N$_2$ = 2:1:22. The samples were fixed in a U-type quartz reactor bed, heated to 220 °C for Cu$_2$O-8 or 205 °C for Cu$_2$O-12 by 2 °C/min and kept for 30 min. The samples were cooled down to the temperature in pure N$_2$.

2.1.3. Inverse model CeO$_2$/Cu$_2$O catalysts

In this step, Cu$_2$O and Ce(NO$_3$)$_3$·6H$_2$O were ultrasonically dispersed in 300 mL of DI water, stirred at 60 °C for 1 h. The ratio of CeO$_2$:Cu$_2$O was fixed at 5:1000 by weight. Then, NaOH solution (0.06 mol/L) was dripped into above mixture. After being stirred at 60 °C for another hour, the precipitate was washed with DI water and ethanol and dried in

vacuum at 60 ℃ for 12 h.

2.2. Characterization

The crystalline structures were investigated by X-ray diffraction analysis (XRD, Shimadzu XRD-6100 X-ray diffractometer). The morphology and surface element distribution were observed by field-emission scanning electron microscope coupled with energy dispersive spectroscopy (FESEM-EDS, Zeiss sigma 5000-Oxford X-MAX). The surface element composition and chemical valence were identified by X-ray photoelectron spectroscopy (XPS, Thermo Scientific Escalab 250 Xi). And the chemical properties were explored by temperature-programed experiments including Temperature-programed reduction of H_2 and Temperature-programed desorption of O_2 (H_2-TPR and O_2-TPD, Micromeritics Auto Chem II2920). Before each experiment, the catalyst was purged under a flow of Ar gas (30 mL/min) at 300 ℃ for 30 min and then cooled to 50 ℃. With respect to H_2-TPR, the gas flow was switched to a 10% H_2/Ar mixture (30 mL/min) and heated to 600 ℃ (heating rate=10 ℃/min). For O_2-TPD, each sample was fully absorbed in a pure O_2 atmosphere at 50 ℃ for 30 min and then exposed in Ar flow to remove physically adsorbed O_2 until the baseline stabilization occurred. The sample is then heated at 10 ℃/min until reaching 1000 ℃.

2.3. Kinetic experiment

Typically, 200 mg of sample was pressed into sheet and sieved into 100–120 mesh (0.1–0.15 mm), which was then mixed with 200 mg of quartz grains (100–120 mesh). At a heating speed of 10 ℃/min, the CO conversion curves were recorded under different O_2 concentration (1%, 3%, 5%, 7% and 10%). During the whole procedure, the CO conversion rate was below 10% and CO concentration was fixed at 10%. Likewise, O_2 concentration was subsequently fixed at 10% and the data were collected when CO concentration was switched from 1% to 10%.

The reaction rate of CO self-sustained combustion is determined by the equation:

$$r_{CO} = \frac{N_{CO} \times X_{CO}}{W_{cat}} \tag{1}$$

Here, r_{CO}, X_{CO}, N_{CO} and W_{cat} represent the reaction rate ($mol_{CO} \bullet g_{cat}^{-1} \bullet s^{-1}$), CO conversion rate (%), molar flow ($mol \bullet s^{-1}$) and the mass of the catalyst (g).

According to law of mass action, the typical kinetic model of CO self-sustained combustion over the catalyst can be described as:

$$r_{CO} = k \times P_{CO}^a \times P_{o_2}^b \tag{2}$$

Here, k, P, a and b respectively represent the reaction rate constant (s^{-1}), the partial pressure (kPa) and the reaction order for CO and O_2.

2.4. Self-sustained catalytic combustion activity in high CO concentration

The sample (200 mg) was pressed into sheet and sieved into 20–40 mesh before loaded into a 10 mm inner diameter U-tube quartz micro reactor. A mixed gas stream of 10% CO + 10% O_2/N_2 was introduced into the reactor with the total flow controlled at 200 mL/min (GHSV=70000 h^{-1}) by a mass flow controller. The reactor was heated from room temperature at a speed of 10 ℃/min until CO signal could not be detected by the CO gas analyzer, which indicates that CO was completely converted into CO_2. There were two 0.5 mm K-type thermocouples equipped, one of which was inserted into the quartz tube to monitor the reaction temperature and the other of which was fixed in the center of the furnace to control the furnace temperature. After the self-sustained combustion was reached, the temperature distribution on the surface of reactor bed was monitored by a forward-looking infrared radiometer (FLIR-T640), with the glass emission rate fixed at 0.87.

2.5. In-situ infrared spectra

In situ infrared (IR) spectra are recorded on a on the FOLI10-R instrument (INSA Optics Instruments (Shanghai) Ltd.), which was equipped with a self-designed magnetically-driven transmission cell and an MCT detector in a resolution of 4 cm^{-1}. Approximately 5 mg of catalyst and 45 mg KBr were mixed and pressed into a self-supporting wafer, followed by pretreatment in pure N_2 flow (30 mL/min) for 1 h at 200 ℃. Then a baseline was collected under the room temperature. The gas flow was thereafter switched to 25% CO+ 25% O_2/N_2 for at least half an hour to ensure the sample was saturated. Following that, the data curves were recorded every 1 min with the temperature rising from room temperature to 500 ℃ at 10 ℃/min.

3. Results and discussion

3.1. XRD, SEM-EDS and XPS analysis

It will be readily apparent from Fig. 1A that diffraction patterns of inverse $CeCu_2$ catalysts conform well with those of typical Cu_2O. Characteristic diffraction peaks emerging at 29.6, 36.5, 42.4, 61.5 and 73.7° can be designated to Bragg reflections of (1 1 0), (1 1 1), (2 0 0), (2 2 0) and (3 1 1) crystal planes of Cu_2O (JCPDS #99–0041), respectively. No other copper species like CuO or Cu^0 are detected and there is also no presence of CeO_2 with fluorite structure in the patterns due to its low loading ratio (theoretically 0.5 wt% CeO_2), which is below the detection limit. It can be tentatively concluded that the catalysts have been successfully prepared and loading of cerium seems not to have adverse effect on the crystal structure. Additionally, the (1 1 1) peaks were compared in Fig. 1B, from which it can be seen that peaks of $CeCu_2$ show a slight shift towards the small angle ($\Delta 2\theta$=0.06° for cubes and 0.08° for both octahedra and dodecahedra) with decreased intensity (ΔI=541, 936 and 707, respectively), indicating the expanded lattice space and weakened crystallinity [23]. The change in lattice parameters has been reported by many researches involving Cu-Ce catalysts and it originates from the synergistic effect between copper and cerium [24,25]. When cerium ions are incorporated by lattice cell of CuO_x, the difference in ion radii of copper and cerium leads to the formation of lattice distortion and an abundant number of oxygen vacancies, changing the lattice parameters [24,26]. The difference in parameter changes implies that the synergistic effect may vary among catalysts.

From the SEM images (Fig. 2A-C), all the as-synthesized catalysts have presented ideal morphology, consisting perfectly with what is expected and respectively exposing six (1 0 0) crystal planes (Fig. 2A), eight (1 1 1) planes (Fig. 2B) and twelve (1 1 0) planes (Fig. 2C) [27]. In Fig. 2A2-C2, noticeable particles growing on the surface can be apparently identified as loaded CeO_2 particles in contrast to Fig.2A1-C1 and the catalysts are observed to remain their regular morphology after the loading. In addition, EDS images (Fig.2D1-D3) have shown a homogenous distribution of surface elements. Due to the low loading ratio of cerium, its distribution cannot be clearly distinguished from the pictures, which may cause the inaccuracy of the loading ratio. Therefore, the precise loading ratio was estimated by ICP-MS as shown in Table 1, which follows $CeCu_2$-8 (0.46%)>$CeCu_2$-12(0.36%)>$CeCu_2$-6(0.31%). The results suggests that CeO_2 may have different binding strength and synergistic effect with crystal planes.

With the assistance of XPS analysis, the composition of chemical elements (Cu, Ce and O) on the surface of inverse $CeCu_2$ catalysts has been revealed in Fig. 3. In Fig. 3A, four major characteristic peaks in Cu 2p spectra can be distinguished, concretely evidencing that bivalent copper coexists with monovalent copper on the surface. Specifically, peaks situated at 932.5 and 952.4 eV (areas filled with light color) are characteristic of Cu^+ $2p_{3/2}$ and $2p_{1/2}$ due to the orbit-spinning and those located at 934.3 and 954.2 eV are feature of Cu^{2+} $2p_{3/2}$ and $2p_{1/2}$ [28, 29]. It should be noted that the location of Cu^+ and Cu^0 are too close to depart in the Cu 2p spectra, thus the Auger electron spectroscopy was
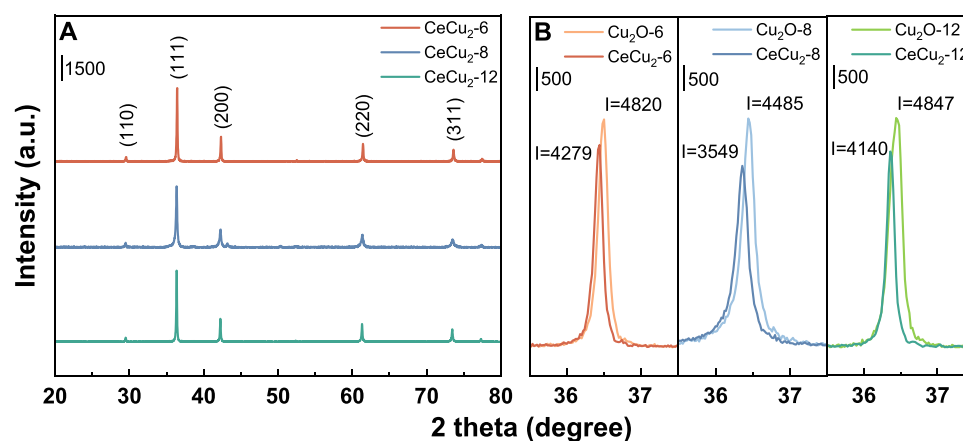
Fig. 1. XRD patterns of (A) CeCu$_2$ catalysts and (B) comparison of all (1 1 1) peaks.
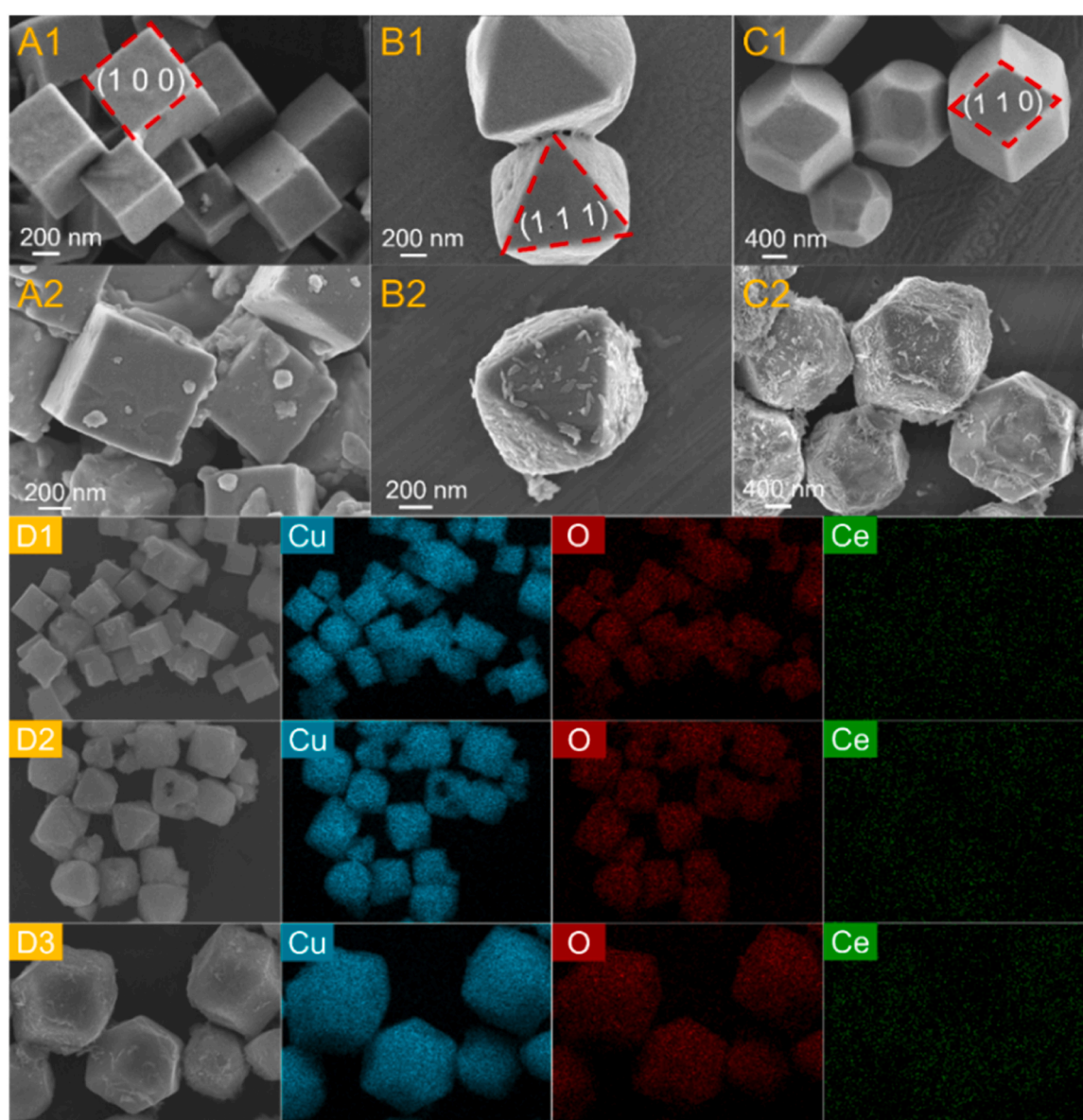

Fig. 2. SEM images of (A1) Cu$_2$O-6, (A2) CeCu$_2$-6, (B1) Cu$_2$O-8, (B2) CeCu$_2$-8, (C1) Cu$_2$O-12 and (C2) CeCu$_2$-12; EDS-mapping images of (D1) CeCu$_2$-6, (D2) CeCu$_2$-8 and (D3) CeCu$_2$-12.

Table 1
Loading ratio of CeO$_2$ by ICP-MS.

Catalyst	Cerium concentration (ppb)	Loading ratio (wt%)
CeCu$_2$-6	83.13	0.31
CeCu$_2$-8	124.14	0.46
CeCu$_2$-12	98.06	0.36

used to distinguish Cu$^+$ from Cu^0. As can be seen in Fig. 3B, there is only one apparent peak at around 916.4 eV (917.4 eV for CeCu$_2$-8), which indicates that no Cu^0 exists in the system since it is widely acknowledged that Cu$^+$ and Cu^0 are situated at 916.7 eV and 918.4 eV [30]. The content of copper is semi-quantified by the spectra and Table 2 gives information that a large quantity of Cu$^+$ dominates in the system. The existence of Cu^{2+} may arise from a minority of Cu$^+$ oxidized to Cu^{2+} during the preparation process. Given the fact that there is no diffraction peak of CuO in XRD analysis, the particles of oxidized Cu^{2+} in CuO should be quite few and this factor can be ignored [31]. A tiny amount of Cu^{2+} may be the residue that was not reduced during the preparation process [32–34]. Apart from these, the majority of Cu^{2+} should be produced by the synergistic effect between copper and cerium. As is reported, when Cu$_2$O interacts with CeO$_2$, the electron transfer from the former to the latter leads to a redox equilibrium of Cu$^+$+Ce^{4+}↔Cu^{2+}+Ce^{3+} [35,36], which is universally acknowledged as the nature of the synergism [37,38]. The ratio of Cu^{2+}/Cu$^+$ drops by the order of CeCu$_2$-8(0.64)>CeCu$_2$-12(0.61)>CeCu$_2$-6(0.46). The decrease in the number of Ce^{3+} and Cu^{2+} implies the weakness in synergistic effect [37].
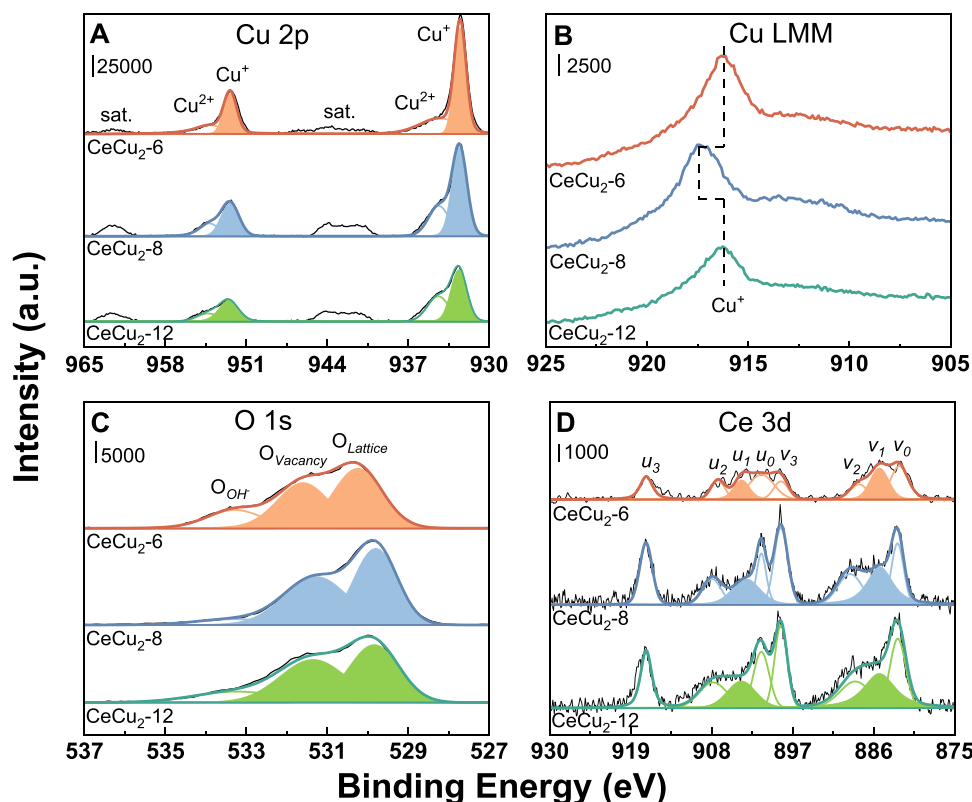
For O 1 s spectra, it can be deconvoluted into three contributions that can be assigned to three kinds of oxygen in distinct chemical states. As has been exhibited in Fig. 3C, the peaks separately with lower binding energy (529.8 eV) and higher binding energy (531.2 eV) are ascribed to lattice oxygen (O^{2-}) labelled as O$_L$ and hydroxyl oxygen (OH$^-$), while the peak with intermediate binding energy (533.3 eV) is indicative of

adsorbed oxygen by vacancies (O$^-$ or O$_2^{2-}$) denoted as O$_V$ [39,40]. Notably, the peaks of O$_L$ and O$_V$ for CeCu$_2$-8 (529.8 eV/531.2 eV) have shifted more to lower position than those for CeCu$_2$-12 (529.9 eV/531.4 eV) and CeCu$_2$-6 (530.2 eV/531.6 eV) owing to the synergistic effect. The lattice distortion and electron transfer caused by such an effect can effectively lower the energy for oxygen to release and facilitate the mobility of oxygen [41]. Furthermore, it promotes the formation of massive oxygen vacancies [42] and reinforces the capture and activation of oxygen [43,44]. The result evidences that CeCu$_2$-8 may have the strongest synergistic effect with the highest concentration of O$_V$ (0.97) in Table 2.

As is depicted in Fig. 3D, there is a typical distribution of characteristic peaks for Ce^{4+} and Ce^{3+}. Here, *u* and *v* are used to mark Ce 3d$_{5/2}$ and 3d$_{3/2}$ spin-orbit doublets. Amongst all the peaks, u_1 (903.3 eV) and v_1 (885.1 eV) are classified to Ce^{3+} while the rest of peaks u_0 (916.9 eV), u_2 (907.9 eV), u_3 (901.2 eV), v_0 (898.6 eV), v_2 (889.2 eV) and v_3 (882.7 eV) can be sorted to Ce^{4+} [25,35,45]. The coexistence obviously sources from the synergistic effect as has been mentioned before. CeO$_2$ has a stronger ability of accepting electrons on account of the electron distribution of Ce^{4+} 4 f^0 5d^0 6 s^0. The effect makes electrons transferred from Cu$_2$O to CeO$_2$ to form the redox equilibrium and weakens the strength of Cu-O bonds by decreasing the electron density of them. Therefore, inferred from its excellent content of Ce^{3+}/Ce^{4+}(0.44), which is higher than that of CeCu$_2$-12 (0.41) and CeCu$_2$-6 (0.38), CeCu$_2$-8

Table 2
Surface element composition of inverse CeCu$_2$ catalysts.

Catalyst	Cu (at %)	Cu^{2+}/Cu$^+$	O (at%)	O$_V$/O$_L$	Ce (at %)	Ce^{3+}/Ce^{4+}
CeCu$_2$-6	16.40	0.46	26.72	0.79	0.71	0.38
CeCu$_2$-8	31.29	0.64	39.71	0.97	1.72	0.44
CeCu$_2$-12	20.00	0.61	34.82	0.91	1.69	0.41

Fig. 3. XPS spectra of (A) Cu 2p, (C) O 1 s, (D) Ce 3d and AES spectra of Cu LMM (B).

should manifest a stronger synergistic effect.

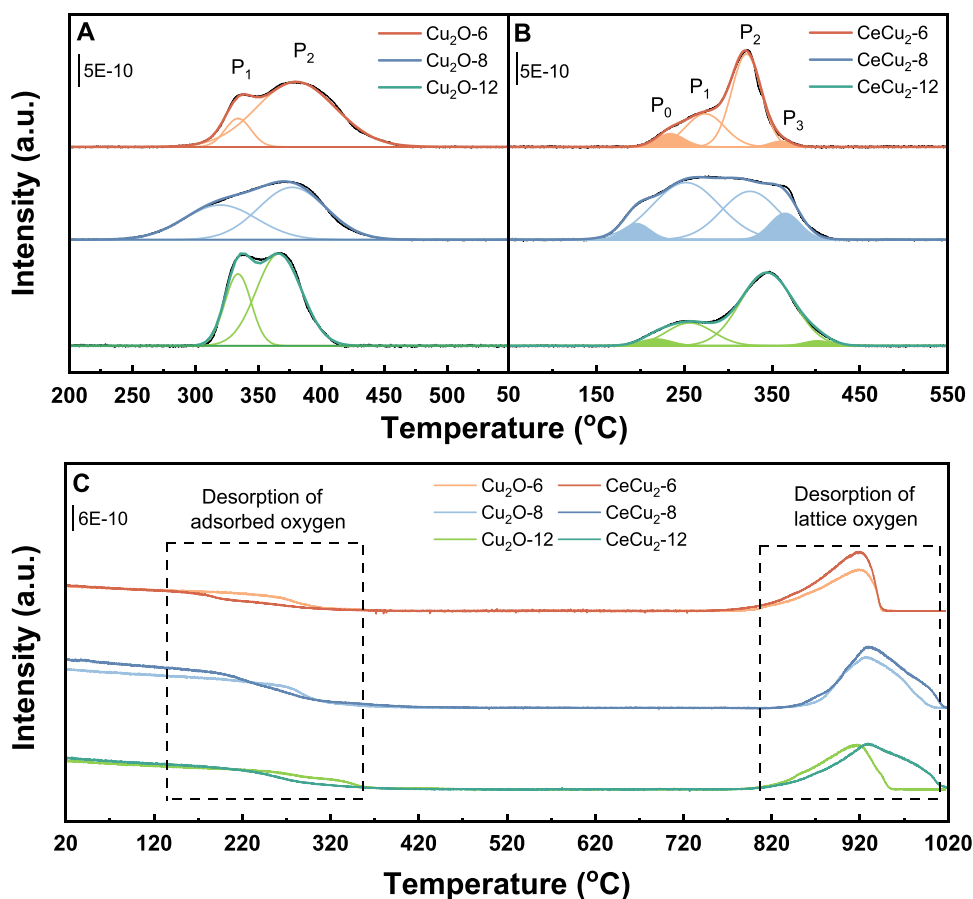## 3.2. Programmed-temperature thermal analysis

The reducibility of catalysts is directly correlative to the catalytic performance in terms of CO self-sustained combustion. Therefore, the H_2-TPR experiments were conducted and the results are displayed in Fig. 4. According to Fig. 4A, there are two main peaks showing up during the reduction, which are correspondingly tagged as P_1 and P_2. For pure Cu_2O catalysts, the reduction peaks are generally recognized as symbols of reduction process of Cu^+ [46]. The former (P_1) is ascribed to the reduction of Cu^+ on the surface and the latter (P_2) is attributed to the reduction of Cu^+ in the lattice cell [37]. In contrast, after the loading of CeO_2, a discernable distinction can be found in Fig. 4B that inverse $CeCu_2$ catalysts exhibit two extra faint reduction peaks labelled as P_0 and P_3, referring to the reduction of two kinds of new species. P_0 with the lowest reduction temperature can be reasonably ascribed to the reduction of Cu^+ interacted with cerium on the Cu-Ce interface [26], since the weakened Cu-O bonds by the synergistic effect are prone to be broken and react with hydrogen. The presence of P_0 contributes to the drop in ignition temperature because the ignition process is dominated by the synergistic effect on the Cu-Ce interface [7] and the lowest P_0 temperature of $CeCu_2$-8 indicates that it owns the most-facilitated ignition temperature. Although Cu^{2+} is observed in Cu 2p spectra and it can also be reduced in hydrogen steam, there are only Cu^+-CO intermediates with no signs of Cu^{2+}-CO intermediates in in-situ IR spectra (see Section 3.5), which suggests that Cu^+ is more active than Cu^{2+} in the system and Cu^{2+} should make no contribution to the reaction. Moreover, it can be inferred that P_3 with the highest reduction temperature can be described as the reduction process of CeO_2 due to the fact that reduction of pure CeO_2 normally occurs at high temperature (above 350 °C) [24]. From Table 3, inverse $CeCu_2$ catalysts have lower reduction temperature with higher H_2 consumption than pure Cu_2O catalysts, which obviously results from the synergistic effect as it weakens the bond strength of Cu-O, making a facile broken of bond and an easy reduction by H_2 [38]. Amongst all the catalysts tested, $CeCu_2$-8 shows a much more outstanding reducibility than its counterpart with lowest ignition temperature (P_0 =196 °C) and Cu reduction temperature (P_1 =252 °C) as well as the most total H_2 consumption (0.468 mmol/g), implying the interaction on (1 1 1) planes is the strongest.

The curves in Fig. 4C illustrates the oxygen adsorption property of catalysts. As is shown in the picture, there are two distinctive desorption peaks for all the catalysts, which respectively represent the desorption process of two sorts of oxygen species. One with lower temperature (below 400 °C) is attributed to the oxygen adsorbed on the oxygen vacancies, whereas the other with higher temperature (above 800 °C) belongs to the release of lattice oxygen in Cu_2O cell [10,47]. It seems that all of the inverse $CeCu_2$ catalysts tend to desorb oxygen more

Table 3
Peak information for H_2-TPR.

Catalysts	Temperature (°C)				H_2 consumption (mmol/g)
	P_0	P_1	P_2	P_3	
Cu_2O-6	/	334	380	/	0.245
$CeCu_2$-6	234	274	321	360	0.271
Cu_2O-8	/	320	377	/	0.254
$CeCu_2$-8	196	252	325	362	0.468
Cu_2O-12	/	333	366	/	0.250
$CeCu_2$-12	218	256	344	402	0.318

Fig. 4. The H_2-TPR curves of (A) pure Cu_2O and (B) inverse $CeCu_2$. The O_2-TPD curves of (C) all the catalysts. Pretreatment: pure Ar at 300 °C for 30 min; experimental conditions: 5% H_2/Ar or pure O_2 (30 mL/min) at 10 °C/min from 50 to 600 °C or 20–1000 °C; sample quantity: 20 mg.

facilely at low temperature and release oxygen more frequently at high temperature, meaning that they have an advantageous adsorption property for oxygen than corresponding Cu_2O catalysts. Obviously, the synergistic effect has assisted well in the oxygen adsorption property in that it produces more oxygen vacancies and improve the mobility of surface oxygen species [7].

3.3. Kinetic experiment

To reveal the essence of the heat and mass transfer during the self-sustained combustion, kinetic experiment was implemented over inverse $CeCu_2$-8 catalyst. It is obvious from Table 4 that when the partial pressure of O_2 stays constant, the reaction rate surges significantly from 0.57 mol/(g·s)$\times 10^{-6}$ to 4.91 mol/(g·s)$\times 10^{-6}$ as the partial pressure of CO rises from 1.18 kPa to 10.97 kPa. However, when the pressure of CO is sustained, the reaction rate simply grows slightly from 4.58 mol/(g·s)$\times 10^{-6}$ to 4.91 mol/(g·s)$\times 10^{-6}$. Fig. 5 illustrates the correlation between partial pressure of gases and reaction rate. The slope of fitted kinetic lines can be regarded as the reflection of significance to the reaction rate. These results prove that the CO self-sustained combustion over inverse $CeCu_2$ catalysts is mainly controlled by CO concentration. In other words, it is CO adsorption, rather than O_2 adsorption, that is the rate-determining step (RDS) for the reaction. Furthermore, a kinetic model can be calculated by non-linear fitting using polymath 6.1 software with data from Table 4 and Eq. (2). The derived expression is listed below:

$$r_{CO} = 4.679 \times 10^{-7} \times P_{CO}^{0.977} \times P_{O_2}^{0.016} \tag{3}$$

From the kinetic model, the reaction order of oxygen (b) equals 0.016, which is close to zero, considering the systematic error. This means that gaseous oxygen does not directly react with adsorbed CO over the catalyst, for its partial pressure has no influence on the reaction rate. As such, the reaction mechanism should follow Mars-van Krevelen (M-K) mechanism.

3.4. Self-sustained catalytic combustion of CO

The relationship between reaction temperature and CO conversion rate under 10% CO+ 10% O_2 is illustrated in Fig. 6A. It appears that both pure Cu_2O and inverse $CeCu_2$ catalysts have three representative phases of CO self-sustained catalytic combustion, which are induction phase, ignition phase and self-sustained phase, respectively. During induction phase, the CO conversion gently climbs as the temperature rises. When the temperature reaches the ignition point, tremendous heat caused by the reaction leads to a sudden increase in temperature and CO conversion rate (>90%), followed by a kinetic transition from low-rate steady state to high-rate steady state. The self-sustained combustion is subsequently achieved when the CO conversion rate plateaus at 100%. In the self-sustained phase, the heat released by combustion is able to cover the heat loss without heating source and enables the conversion rate to continuously sustain 100% at a certain temperature [7]. The
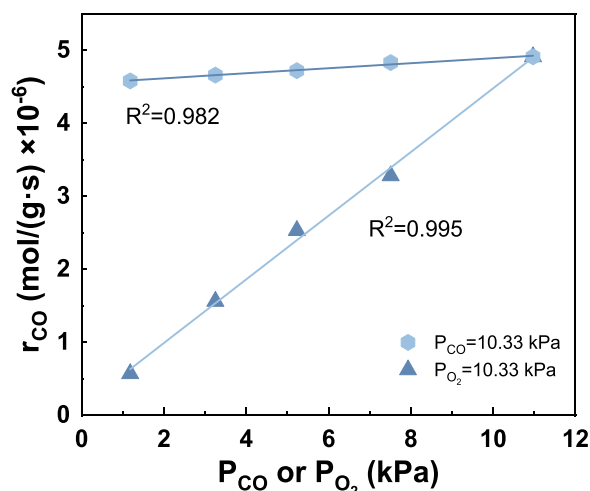
Table 4
Kinetic experiment for inverse $CeCu_2$-8 catalyst.

No.	Partial pressure (kPa)		Conversion (%)	Reaction rate (mol/(g·s) $\times 10^{-6}$)
	CO	O_2		
1	1.18	10.33	10.90	0.57
2	3.25	10.33	8.57	1.56
3	5.23	10.33	7.56	2.53
4	7.51	10.33	6.78	3.28
5	10.97	10.33	6.28	4.91
6	10.33	1.18	5.87	4.58
7	10.33	3.25	5.96	4.66
8	10.33	5.23	6.04	4.72
9	10.33	7.51	6.18	4.83
10	10.33	10.97	6.28	4.91

Fig. 5. Fitted kinetic lines for inverse $CeCu_2$-8 catalyst.

ignition temperature (T_{10}) is defined as the temperature where CO conversion rate reaches 10% and it was found to be lowered to some extent in $CeCu_2$ catalysts, following the order of $CeCu_2$-8(173 ℃) <$CeCu_2$-12(181 ℃)<Cu_2O-8(184 ℃)<Cu_2O-12(190 ℃)<$CeCu_2$-6 (194 ℃)<Cu_2O-6(200 ℃). This is clearly due to the synergistic effect that dominates the ignition on the Cu-Ce interface, which has been verified in H_2-TPR part. After realizing the stable self-sustained combustion, the catalytic activity (T_{90}) is subject to the temperature at which the CO conversion rate reaches 90% and they can be ranked as $CeCu_2$-8(185 ℃)>$CeCu_2$-12(193 ℃)>$CeCu_2$-6(207 ℃)>Cu_2O-8(214 ℃) >Cu_2O-12(218 ℃)>Cu_2O-6(236 ℃). Fig. 6B has shown the temperature distribution of the reactor bed during self-sustained phases, where the reaction process is totally associate with the exposed crystal planes of Cu_2O. It is seen that the corresponding hot zone temperature is 303.3, 331.2 and 335.4 ℃, respectively. Moreover, combined with the obtained activity curves, the activation energy (E_a) of pure Cu_2O and inverse $CeCu_2$ catalysts was calculated and depicted in Fig. 6C. As expected, $CeCu_2$-8 has lower activation energy (54.32 kJ/mol) than $CeCu_2$-12 (57.81 kJ/mol) and $CeCu_2$-6 (70.09 kJ/mol) and this means a more favorable process of self-sustained combustion as well as a better activity. Also, the activation energy of inverse $CeCu_2$ catalysts has been decreased compared with corresponding pure Cu_2O catalysts with ΔE_a= 6.56 kJ/mol (between cubes), 9.41 kJ/mol (between octahedra) and 8.27 kJ/mol (between dodecahedra), owing to the synergistic effect. Besides, SEM images in Fig. 7 exhibit the morphology of used catalysts, from which it can be seen that a dense part of surface Cu_2O have been oxidized to supply the extra active sites and the surfaces are covered by a layer of CuO, due to the rapid and steady adsorption-release equilibrium of activated oxygen to participate in the combustion with excessive oxygen [48]. Nonetheless, the crystal structure of $CeCu_2$ can be still identified after the test, which manifests a stable and predominant performance.

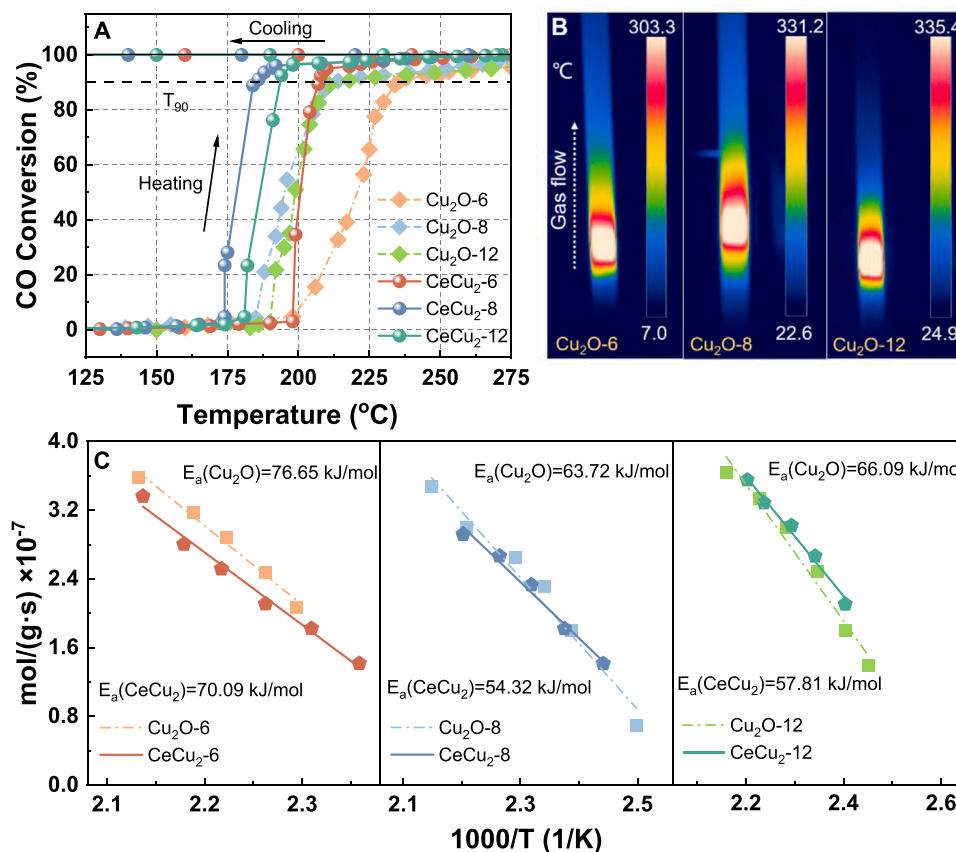Predictably, the self-sustained combustion activity of inverse $CeCu_2$ catalysts is remarkably promoted in contrast to pure Cu_2O catalysts, which can be discussed from two main aspects. For one thing, the distribution of Cu and O atoms individually varies on different exposed crystal planes of Cu_2O, thus exhibiting distinguishing properties due to its structure sensitivity. As shown in Fig. 8, in regard to (1 0 0) plane of cubic catalysts, its outer layer is terminated by two-coordinated O atoms with two-coordinate Cu atoms arranged in the second layer. In this situation, two nearest-neighboring O atoms are not linked by one same Cu atom, which causes difficulty for CO to adsorb on Cu^+ and results in poor self-sustained combustion activity. As for (1 1 0) plane of rhombic dodecahedral catalysts, its outer layer is terminated by three-coordinated O atoms and two-coordinated Cu atoms and two nearest-
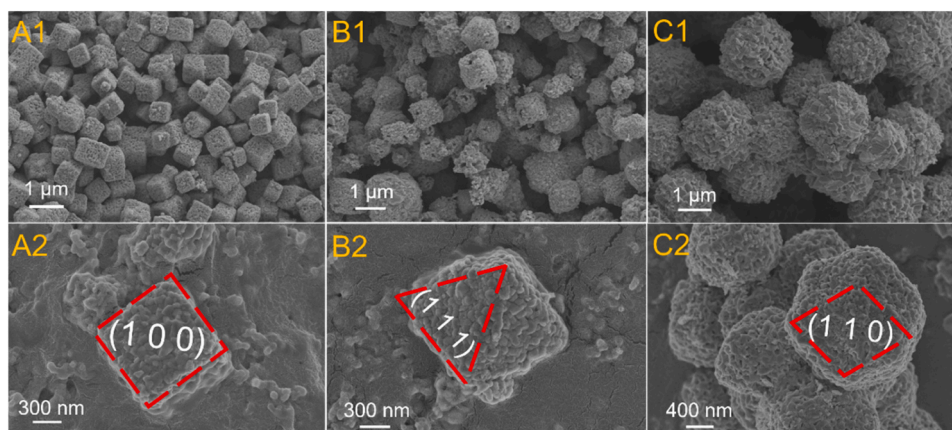
Fig. 6. The picture of (A) catalytic activity, (B) temperature distribution and (C) activation energy of catalysts. Conditions: 10% CO+ 10% O_2 (200 mL/min) at 10 °C/min from 50 to 300 °C; GHSV= 70000 h^{-1}; sample: 200 mg, 20–40 mesh; Pretreatment: pure N_2 at 200 °C for 30 min.
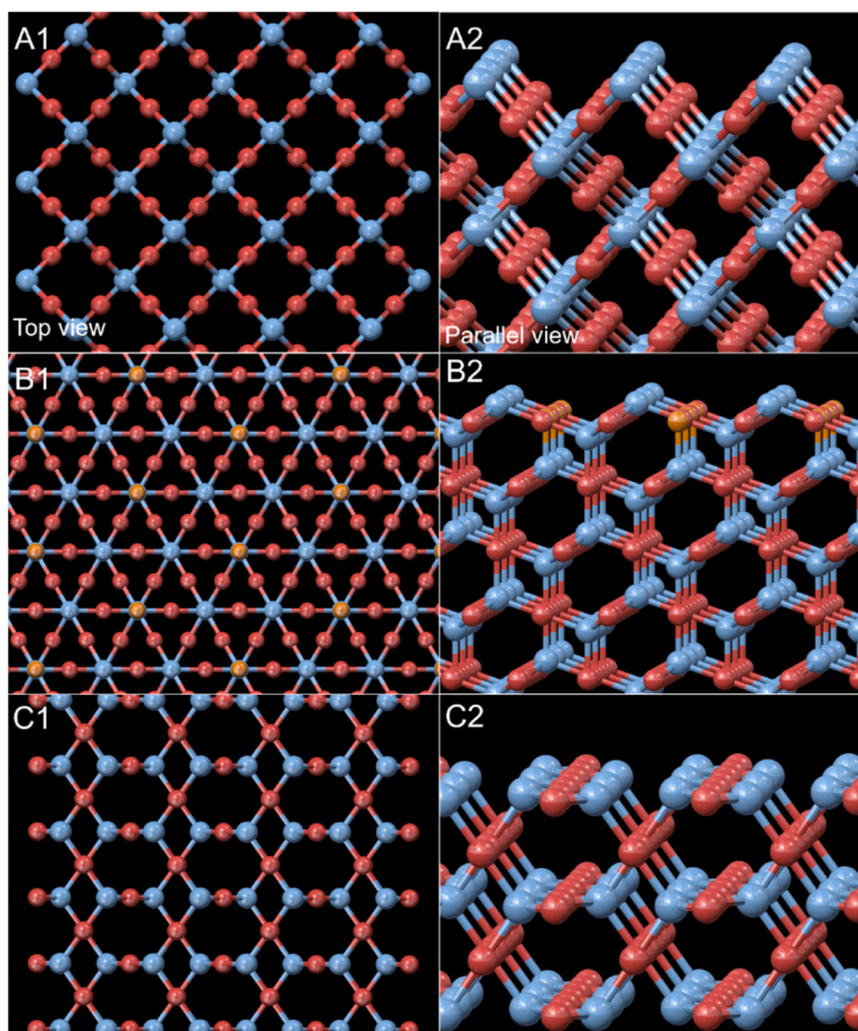

Fig. 7. SEM images of used (A) CeCu$_2$-6, (B) CeCu$_2$-8 and (C) CeCu$_2$-12.

neighboring O atoms are linked by one same Cu atom. Hence, CO can be easily adsorbed on Cu$^+$, which brings a better catalytic activity. In addition, although (1 1 1) plane of octahedral catalysts is terminated by three-coordinated O atoms and two-coordinated Cu atoms, the distance between atoms is long enough to form an open surface structure, which makes it feasible for CO to adsorb on Cu$^+$ atoms in the second layer and 25% of the Cu atoms in the second layer are one-coordinated. During the self-sustained combustion, Cu$^+$ atoms act as the sites to adsorb CO so when the adsorption occurs, due to the electron distribution of Cu$^+$ $3d^{10}$ $4s^0$, empty orbits of Cu$^+$ can receive electrons transferred from CO to form σ-bond and ᴅ-electrons of Cu$^+$ will meanwhile move to CO via back-donation from the surface cation to the anti-π bond orbital,

weakening the bond order of C-O to activate the adsorbed CO. Therefore, unsaturated Cu$^+$ on (1 1 1) can adsorb more CO in that they provide more empty orbits to accept electrons from CO. As a result, (1 1 1) plane with better electron transfer ability performances better on self-sustained combustion than other crystal planes [49].

For another thing, the promotion in activity of inverse CeCu$_2$ catalysts after the loading of CeO$_2$ can also be attributed to the synergistic effect between Cu$_2$O and CeO$_2$, which affects the catalysts in two principal ways. On one hand, When CeO$_2$ is introduced into Cu$_2$O lattice, the radius difference between cerium and copper induces lattice distortion with changed parameters, further producing rich oxygen vacancies [50]. On the other hand, the electron distribution structure of Ce^{4+} $4 f^0 3d^0$

Fig. 8. Atom distribution on (A) Cu_2O-6, (B) Cu_2O-8 and (C) Cu_2O-12. Blue, red and orange balls represent O, coordinately saturated Cu and coordinately unsaturated Cu, respectively.
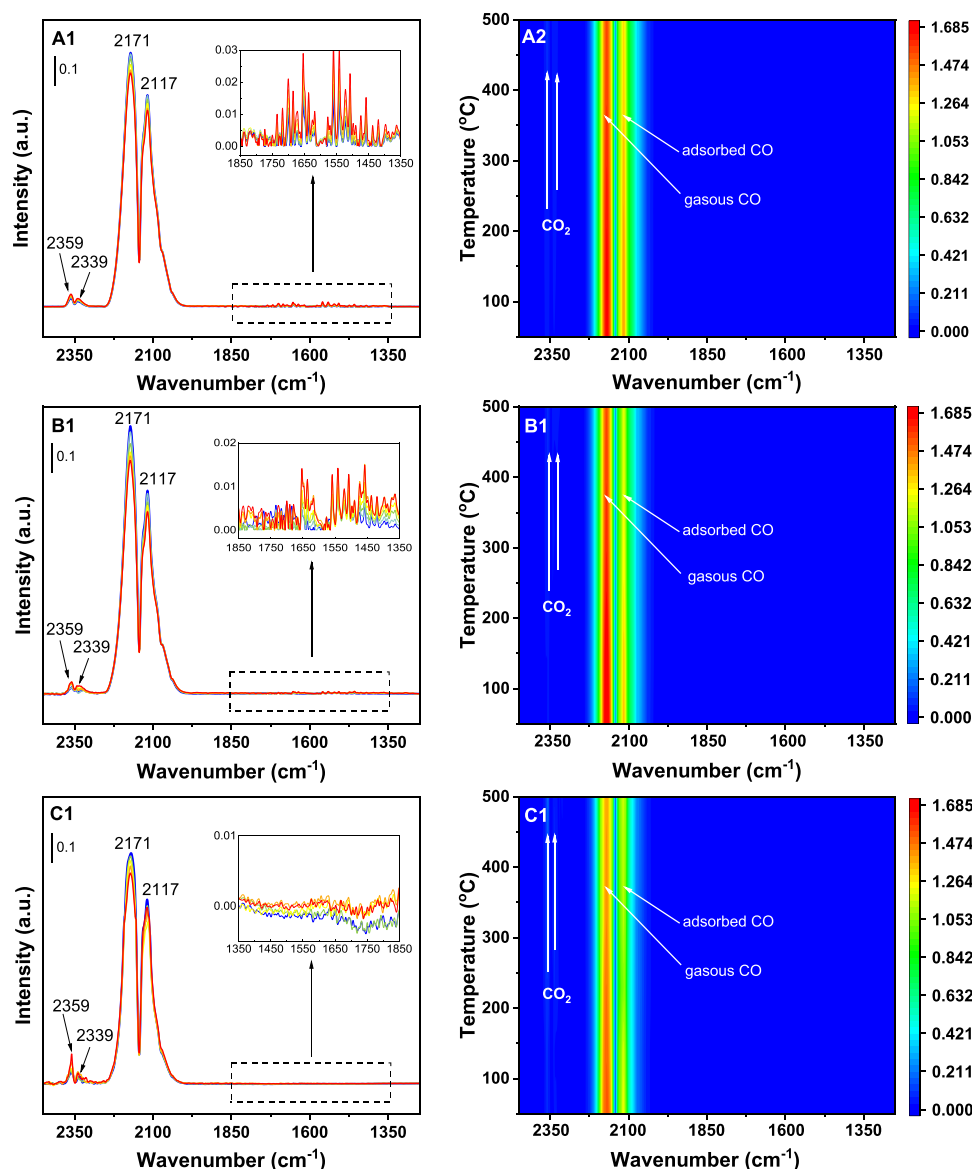
$4 s^0$ makes Ce^{4+} a stronger electron acceptor than Cu^+ because Ce^{4+} can provide relatively more empty orbits. As a consequence, electrons are transferred from Cu^+ to Ce^{4+} and a redox balance of $Cu^++Ce^{4+}\leftrightarrow Cu^{2+}+Ce^{3+}$ is formed [51]. The decline in electron density causes weakened Cu-O bonds and simultaneously leads to an escape of O atoms to form numerous oxygen vacancies easily. It is well known that oxygen vacancies play a crucial role in trapping gaseous oxygen, activating adsorbed oxygen and converting lattice oxygen as well as facilitating the catalytic activity [52]. In both ways, the synergistic effect boosts the formation of oxygen vacancies. For that reason, inverse $CeCu_2$ catalysts exhibits more outstanding catalytic performance than pure Cu_2O catalysts.

Another noticeable thing is that the synergistic effect on every crystal plane has apparently affected the catalysts to varying extents. It appears that the strongest synergistic effect occurs on (1 1 1) plane. O-termination on (1 0 0) inhibits the contact between CeO_2 and Cu_2O as well as the electron transfer between each other, which accounts for the weakest synergistic effect on Cu_2O-6. And it may also explain why CeO_2 on Cu_2O-6 seems like bulk particles in SEM images (Fig. 2A): the difficulty in reaching Cu^+ only allow CeO_2 particles to grow and gather on limited spots. For (1 1 1) and (1 1 0) planes, CeO_2 can directly reach Cu^+ atoms and induce the electron transfer, thus CeO_2 seems to disperse well on the surface in SEM images (Fig. 2B-C). However, the coordinately unsaturated Cu^+ atoms on (1 1 1) are in a less stable state, have weaker constraint to O and tend to bind more CeO_2, bringing more rapid

electron transfer and oxygen vacancies to catalysts. Consequently, the synergistic effect on catalysts follows the order of $CeCu_2$-8>$CeCu_2$-12>$CeCu_2$-6.

3.5. In-situ IR

The in-situ IR spectroscopy was carried out to reveal the reaction mechanism, by detecting the formed intermediates during the CO self-sustained catalytic combustion. In Fig. 9, two intense bands are observed after saturated adsorption. One peak at 2171 cm^{-1} wavenumber can be designated to the gaseous CO [30,53,54], the other one at 2117 cm^{-1} can be attributed to the linear-adsorbed CO by carbonyl bond [48,55,56]. In some studies, the synergistic effect between copper and cerium sometimes may bring about the reconstruction of active sites and discernable change in the wavenumber position for CO adsorption has occurred [7]. However, in this study, the carbonyl has no shift in location, indicating that no new active site, such as Cu-[O]-Ce, has formed and Cu^+ is still the main active site. Moreover, two weak bands are situated at 2359 and 2339 cm^{-1}, which both belong to gaseous CO_2 [52,57]. As the temperature rises, the intensity of 2177 and 2171 cm^{-1} decreases along with that of 2359 and 2339 cm^{-1} increased, showing that adsorbed CO has been converted to CO_2. It can be noticed that $CeCu_2$-6 and $CeCu_2$-8 exhibit faint bands of carbonate species in the range of 1400–1800 cm^{-1} while $CeCu_2$-12 does not. Due to the fact that the outer layers of both $CeCu_2$-6 and $CeCu_2$-8 are terminated by O, a

Fig. 9. In-situ IR spectra and mapping results of inverse (A) CeCu$_2$-6 (B) CeCu$_2$-8 and (C) CeCu$_2$-12 catalysts. Pretreatment: pure N$_2$ at 300 ℃ for 1 h; experimental conditions: 25% CO+ 25% O$_2$ (50 mL/min) from 30 to 500 ℃ at 10 ℃/min; sample: 5 mg + 45 mg KBr; recording interval: 1 min.
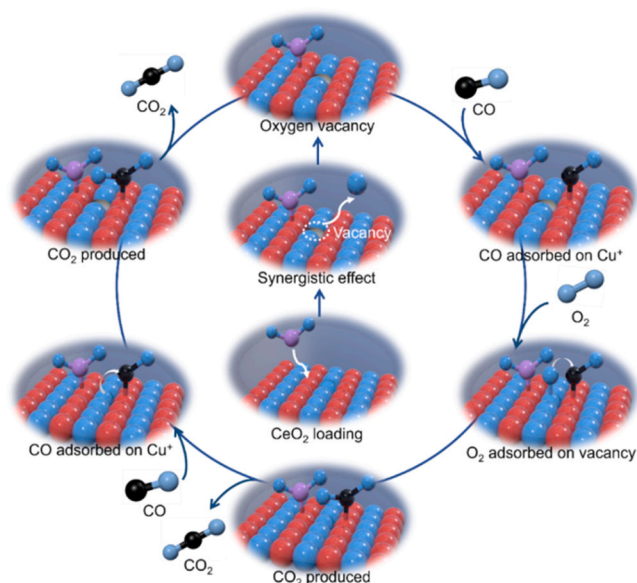
small quantity of CO can be weakly adsorbed on O atoms to form carbonate species but it makes a negligible contribution to producing CO$_2$ [48]. The conclusion coincides well with kinetic experiments, proving that CO self-sustained combustion over inverse CeCu$_2$ catalysts is indeed abided by M-K mechanism.

Combined with the results of the kinetic experiment and in-situ IR spectra, the reaction pathway and synergistic effect of CO self-sustained catalytic combustion over inverse CeCu$_2$ catalysts can be proposed as has been vividly illustrated in Fig. 10. When CeO$_2$ is loaded on the surface of Cu$_2$O, by the synergistic effect, oxygen escapes to form oxygen vacancy, which adsorbs and activates the gas O$_2$ into lattice oxygen. Gaseous CO is initially adsorbed on Cu$^+$ site adjacent to the oxygen vacancy and the intermediates of Cu$^+$-CO carbonyl is formed. Subsequently, adsorbed CO reacts with one oxygen atom to produce CO$_2$. After the desorption of CO$_2$, another CO molecule is adsorbed on the same Cu$^+$ site and reacts with the other oxygen atom, leaving the oxygen vacancy to adsorb another O$_2$ molecule, forming a cycle that is widely recognized as M-K mechanism.

4. Conclusion

To summarize, by solution-phase synthesis method and impregnation method, morphological Cu$_2$O and inverse model CeO$_2$/Cu$_2$O catalysts exposing (1 0 0), (1 1 1) and (1 1 0) crystal planes have been successfully prepared to explore the synergistic effect between copper and cerium as well as the reaction mechanism of CO self-sustained catalytic combustion. By comprehensive characterizations such as XRD, SEM, XPS, H$_2$-TPR and O$_2$-TPD, it is revealed that the Cu-Ce interface formed by the synergistic effect can notably decrease the ignition temperature, directly dominating the ignition process. However, after the ignition, the self-sustained combustion is mainly controlled by the heat and mass transfer on crystal planes of Cu$_2$O with abundant lattice oxygen and Cu$^+$ active sites to follow the M-K mechanism. Oxygen vacancy produced by the electron transfer (Cu$^+$+Ce^{4+}↔Cu^{2+}+Ce^{3+}) of the synergistic effect indirectly promotes the adsorption and activation of O$_2$ as well as the catalytic performance of inverse CeCu$_2$ catalysts. Apart from the synergistic effect, exposure of specific crystal planes also benefits CO self-sustained combustion since the surface reaction is highly structure-sensitive. Open surface structure

Fig. 10. CO self-sustained catalytic combustion reaction over inverse catalysts. Red, blue, black and purple balls represent Cu, O, C and Ce, respectively.

and coordinately unsaturated Cu atoms on Cu_2O (1 1 1) contributes to the adsorption and conversion of CO while the structure of O-termination and Cu atom on the second layer of Cu_2O (1 0 0) inhibits the contact with other molecules. As a result, inverse $CeCu_2$-8 (1 1 1) catalysts can manifest the superior reducibility, oxygen adsorption property and facilitated catalytic activity with more oxygen vacancies.

Overall, this approach of inverse model catalysts can be a feasible method to explore the interaction and reaction mechanism on the surface. Focusing on the control of interfacial sites, the inverse model system is able to endow the active materials like Cu_2O with many physicochemical properties distinct from conventional bulk model catalysts, such as grain size and morphology. Due to the small size and low defect density of loaded materials in the conventional model system, the inverse system may provide more controllable effects and strengthened functional site density, which benefits the exploration on the synergistic effect and reaction mechanism. Moreover, during the preparation, apart from the synergistic effect, orientated exposure of specific crystal planes with higher activity is an effective alternative to designing optimized catalysts. Meanwhile, thanks to the identified regular surface structure of the exposed crystal planes, macroscale reaction process on the catalysts can be narrowed down to the interaction between molecules and crystal planes on the microscale, in favor of thorough investigation on the reaction mechanism.

CRediT authorship contribution statement

Zihao Teng: Conceptualization, Methodology, Formal analysis, Investigation, Data curation, Writing – original drafting, Editing, Software. **Xiaokun Yi:** Data curation, Investigation. **Chenhang Zhang:** Data curation, Investigation. **Chi He:** Investigation. **Yulong Yang:** Investigation. **Qinglan Hao:** Supervision. **Baojuan Dou:** Supervision, Project administration, Writing – review & editing. **Feng Bin:** Supervision, Project administration, Writing – review & editing.

Declaration of Competing Interest

The authors declare that they have no known competing financial interests or personal relationships that could have appeared to influence the work reported in this paper.

References

[1] Y. Xie, J. Wu, G. Jing, H. Zhang, S. Zeng, X. Tian, X. Zou, J. Wen, H. Su, C.J. Zhong, P. Cui, Structural origin of high catalytic activity for preferential CO oxidation over CuO/CeO_2 nanocatalysts with different shapes, Appl. Catal. B. 239 (2018) 665–676.

[2] R. Si, J. Raitano, N. Yi, L. Zhang, S.W. Chan, M. Flytzani-Stephanopoulos, Structure sensitivity of the low-temperature water-gas shift reaction on Cu-CeO2 catalysts, Catal. Today 180 (2012) 68–80.

[3] C. Deng, B. Li, L. Dong, F. Zhang, M. Fan, G. Jin, J. Gao, L. Gao, F. Zhang, X. Zhou, NO reduction by CO over CuO supported on CeO_2-doped TiO_2: The effect of the amount of a few CeO_2, Phys. Chem. Chem. Phys. 17 (2015) 16092–16109.

[4] T.S. Cam, T.A. Vishnevskaya, S.O. Omarov, V.N. Nevedomskiy, V.I. Popkov, Urea–nitrate combustion synthesis of CuO/CeO_2 nanocatalysts toward low-temperature oxidation of CO: the effect of Red/O_x ratio, J. Mater. Sci. 55 (2020) 11891–11906.

[5] F. Bin, R.N. Kang, X.L. Wei, Q. Hao, B. Dou, Self-sustained combustion of carbon monoxide over $CuCe_{0.75}Zr_{0.25}O_\delta$ catalyst: stability operation and reaction mechanism, Proc. Combust. Inst. 37 (2019) 5507–5515.

[6] F. Bin, X.L. Wei, B. Li, K.S. Hui, Self-sustained combustion of carbon monoxide promoted by the Cu-Ce/ZSM-5 catalyst in $CO/O_2/N_2$ atmosphere, Appl. Catal. B. 162 (2015) 282–288.

[7] R.N. Kang, P.D. Ma, J.Y. He, H. Li, F. Bin, X. Wei, B. Dou, K.N. Hui, K.S. Hui, Transient behavior and reaction mechanism of CO catalytic ignition over a $CuO–CeO_2$ mixed oxide, Proc. Combus. Inst. 38 (2021) 6493–6501.

[8] A. Younis, D. Chu, S. Li, Cerium oxide nanostructures and their applications, Funct. Nanomater 3 (2016) 53–68.

[9] M. Fronzi, M.H.N. Assadi, D.A.H. Hanaor, Theoretical insights into the hydrophobicity of low index CeO_2 surfaces, Appl. Surf. Sci. 478 (2019) 68–74.

[10] Q. Zou, Y. Zhao, X. Jin, J. Fang, D. Li, K. Li, J. Lu, Y. Luo, Ceria-nano supported copper oxide catalysts for CO preferential oxidation: Importance of oxygen species and metal-support interaction, Appl. Surf. Sci. 494 (2019) 1166–1176.

[11] P. Sudarsanam, B. Hillary, B. Mallesham, B.G. Rao, M.H. Amin, A. Nafady, A. M. Alsalme, B.M. Reddy, S.K. Bhargava, Designing CuO_x nanoparticle-decorated CeO_2 nanocubes for catalytic soot oxidation: role of the nanointerface in the catalytic performance of heterostructured nanomaterials, Langmuir 32 (2016) 2208–2215.

[12] Q. Hua, T. Cao, H.Z. Bao, Z.Q. Jiang, W.X. Huang, Crystal-plane-controlled surface chemistry and catalytic performance of surfactant-free Cu_2O nanocrystals, ChemSusChem 6 (2013) 1966–1972.

[13] Y. Sui, W. Fu, H. Yang, Y. Zeng, Y. Zhang, Q. Zhao, Y. Li, X. Zhou, Y. Leng, M. Li, G. Zou, Low temperature synthesis of Cu_2O crystals: Shape evolution and growth mechanism, Cryst. Growth Des. 10 (2010) 99–108.

[14] W. Huang, Oxide nanocrystal model catalysts, Acc. Chem. Res. 49 (2016) 520–527.

[15] D. Wang, M. Mo, D. Yu, L. Xu, F. Li, Y. Qian, Large-scale growth and shape evolution of Cu_2O cubes, Cryst. Growth Des. 3 (2003) 717–720.

[16] L. Wu, P. Ma, C. Zhang, X. Yi, Q. Hao, B. Dou, F. Bin, Effects of Cu_2O morphology on the performance of CO self-sustained catalytic combustion, Appl. Catal. A: Gen. 652 (2023).

[17] J.A. Rodríguez, J. Hrbek, Inverse oxide/metal catalysts: a versatile approach for activity tests and mechanistic studies, Surf. Sci. 604 (2010) 241–244.

[18] A.P. Jia, S.Y. Jiang, J.Q. Lu, M.F. Luo, Study of catalytic activity at the $CuO-CeO_2$ interface for CO oxidation, J. Phys. Chem. C. 114 (2010) 21605–21610.

[19] J. Li, Z. Ni, Y. Ji, Y. Zhu, H. Liu, Y. Zhang, X.Q. Gong, Z. Zhong, F. Su, ZnO supported on Cu_2O{1 0 0} enhances charge transfer in dimethyldichlorosilane synthesis, J. Catal. 374 (2019) 284–296.

[20] J. Qi, J. Chen, G. Li, S. Li, Y. Gao, Z. Tang, Facile synthesis of core-shell $Au@CeO_2$ nanocomposites with remarkably enhanced catalytic activity for CO oxidation, Energy Environ. Sci. 5 (2012) 8937–8941.

[21] J.A. Rodriguez, J. Graciani, J. Evans, J.B. Park, F. Yang, D. Stacchiola, S. D. Senanayake, S. Ma, M. Perez, P. Liu, J.F. Sanz, J. Hrbek, Water-gas shift reaction on a highly active inverse $CeO_x/Cu(111)$ catalyst: unique role of ceria nanoparticles, Angew. Chem. Int. Ed. 48 (2009) 8047–8050.

[22] A. Hornés, A.B. Hungría, P. Bera, A. López Cámara, M. Fernández-García, A. Martínez-Arias, L. Barrio, M. Estrella, G. Zhou, J.J. Fonseca, J.C. Hanson, J. A. Rodriguez, Inverse CeO_2/CuO catalyst as an alternative to classical direct configurations for preferential oxidation of CO in hydrogen-rich stream, J. Am. Chem. Soc. 132 (2010) 34–35.

[23] Y. Lu, L. Duan, Z. Sun, J. Chen, Flame spray pyrolysis synthesized $CuO-CeO_2$ composite for catalytic combustion of C_3H_6, Proc. Combust. Inst. 38.4 (2021) 6651–6660.

[24] X. Zhang, L. Su, Y. Kong, D. Ma, Y. Ran, S. Peng, L. Wang, Y. Wang, CeO_2 nanoparticles modified by CuO nanoparticles for low-temperature CO oxidation with high catalytic activity, J. Phys. Chem. Solids 147 (2020), 109651.

[25] W. Jie, Y. Liu, W. Deng, Q. Liu, M. Qiu, S. Liu, J. Hu, L. Gong, Effect of one-dimensional ceria morphology on CuO/CeO$_2$ catalysts for CO preferential oxidation, J. Solid State Chem. 311 (2022), 123109.

[26] S.T. Hossain, E. Azeeva, K. Zhang, E.T. Zell, D.T. Bernard, S. Balaz, R. Wang, A comparative study of CO oxidation over Cu-O-Ce solid solutions and CuO/CeO$_2$ nanorods catalysts, Appl. Surf. Sci. 455 (2018) 132–143.

[27] Q. Hua, T. Cao, X.-K. Gu, J. Lu, Z. Jiang, X. Pan, L. Luo, W.-X. Li, W. Huang, Crystal-plane-controlled selectivity of Cu$_2$O catalysts in propylene oxidation with molecular oxygen, Angew. Chem. 126 (2014) 4956–4961.

[28] X.L. Pang, H.Y. Bai, D.B. Xu, J. Ding, W. Fan, W. Shi, Dual-functional electrochemical bio-sensor built from Cu$_2$O for sensitively detecting the thiols and Hg^{2+}, Appl. Surf. Sci. 564 (2021), 150397.

[29] T.S. Cam, S.O. Omarov, M.I. Chebanenko, A.S. Sklyarova, V.N. Nevedomskiy, V. I. Popkov, One step closer to the low-temperature CO oxidation over non-noble CuO/CeO$_2$ nanocatalyst: The effect of CuO loading, J. Environ. Chem. Eng. 9 (2021), 105373.

[30] W.X. Zou, L.C. Liu, L. Zhang, L. Li, Y. Cao, X. Wang, C. Tang, F. Gao, L. Dong, Crystal-plane effects on surface and catalytic properties of Cu$_2$O nanocrystals for NO reduction by CO. Appl. Catal. A Gen. 505 (2015) 334–343.

[31] B.Q. Liu, X. Yao, Z.J. Zhang, C. Li, J. Zhang, P. Wang, J. Zhao, Y. Guo, J. Sun, C. Zhao, Synthesis of Cu$_2$O nanostructures with tunable crystal facets for electrochemical CO$_2$ reduction to alcohols, ACS Appl. Mater. Interfaces 13 (2021) 39165–39177.

[32] D.A. Svintsitskiy, L.S. Kibis, A.I. Stadnichenko, V.I. Zaikovskii, S. v Koshcheev, A. I. Boronin, Reactivity and thermal stability of oxidized copper clusters on the tantalum(V) oxide surface, Kinet. Catal. 54 (2013) 497–504.

[33] H.Y. Niu, S.L. Liu, Y.Q. Cai, F. Wu, X. Zhao, MOF derived porous carbon supported Cu/Cu$_2$O composite as high performance non-noble catalyst, Microporous Mesoporous Mater. 219 (2016) 48–53.

[34] Z.H. Dan, J.F. Lu, F. Li, F. Qin, H. Chang, Ethanol-mediated 2D growth of Cu$_2$O nanoarchitectures on nanoporous Cu templates in anhydrous ethanol, Nanomaterials 8 (2017) 18.

[35] S.B. Khan, K. Akhtar, E.M. Bakhsh, A.M. Asiri, Electrochemical detection and catalytic removal of 4-nitrophenol using CeO$_2$-Cu$_2$O and CeO$_2$-Cu$_2$O/CH nanocomposites, Appl. Surf. Sci. 492 (2019) 726–735.

[36] Y. Zeng, Y. Wang, F. Song, S. Zhang, Q. Zhong, The effect of CuO loading on different method prepared CeO$_2$ catalyst for toluene oxidation, Sci. Total Environ. 712 (2020), 135635.

[37] F. Zhao, S. Li, X. Wu, R. Yue, W. Li, X. Zha, Y. Deng, Y. Chen, Catalytic behaviour of flame-made CuO-CeO$_2$ nanocatalysts in efficient CO oxidation, Catalysts 9 (2019) 256.

[38] C.S. Polster, H. Nair, C.D. Baertsch, Study of active sites and mechanism responsible for highly selective CO oxidation in H$_2$ rich atmospheres on a mixed Cu and Ce oxide catalyst. J. Catal. 266 (2009) 308–319.

[39] Q. Yuan, L. Chen, M. Xiong, J. He, S.L. Luo, C.T. Au, S.F. Yin, Cu$_2$O/BiVO$_4$ heterostructures: synthesis and application in simultaneous photocatalytic oxidation of organic dyes and reduction of Cr(VI) under visible light, Chem. Eng. J. 255 (2014) 394–402.

[40] S. Li, H. Wang, W. Li, X. Wu, W. Tang, Y. Chen, Effect of Cu substitution on promoted benzene oxidation over porous CuCo-based catalysts derived from layered double hydroxide with resistance of water vapor, *Appl. Catal. B.* 166– 167 (2015) 260–269.

[41] R. Zhang, W.Y. Teoh, R. Amal, B. Chen, S. Kaliaguine, Catalytic reduction of NO by CO over Cu/Ce$_x$Zr$_{1-x}$O$_2$ prepared by flame synthesis, J. Catal. 272 (2010) 210–219.

[42] C.Y. Ge, J.F. Sun, Q. Tong, W. Zou, L. Li, L. Dong, Synergistic effects of CeO$_2$/Cu$_2$O on CO catalytic oxidation: electronic interaction and oxygen defect, J. Rare Earths (2021) 1211–1218.

[43] H.R. Li, J.Y. Tian, F. Xiao, R. Huang, S. Gao, F. Cui, S. Wang, X. Duan, Structure-dependent catalysis of cuprous oxides in peroxymonosulfate activation via nonradical pathway with a high oxidation capacity, J. Hazard Mater. 385 (2020), 121518.

[44] X.J. Yu, J. Zhang, Y.Y. Chen, Q. Ji, Y. Wei, J. Niu, Z. Yu, B. Yao, Ag-Cu$_2$O composite films with enhanced photocatalytic activities for methylene blue degradation: analysis of the mechanism and the degradation pathways, J. Environ. Chem. Eng. 9 (2021), 106161.

[45] Y. Pu, Y.D. Luo, X.Q. Wei, J. Sun, L. Li, W. Zou, L. Dong, Synergistic effects of Cu$_2$O-decorated CeO$_2$ on photocatalytic CO$_2$ reduction: Surface Lewis acid/base and oxygen defect, Appl. Catal. B 254 (2019) 580–586.

[46] C. Qi, Y. Zheng, H. Lin, H. Su, X. Sun, L. Sun, CO oxidation over gold catalysts supported on CuO/Cu$_2$O both in O$_2$-rich and H$_2$-rich streams: Necessity of copper oxide, Appl. Catal. B. 253 (2019) 160–169.

[47] Y. Yang, S.Z. Zhang, S.W. Wang, K. Zhang, H. Wang, J. Huang, S. Deng, B. Wang, Y. Wang, G. Yu, Ball milling synthesized MnO$_x$ as highly active catalyst for gaseous POPs removal: significance of mechanochemically induced oxygen vacancies, Environ. Sci. Technol. 49 (2015) 4473–4480.

[48] R.N. Kang, J.Q. Huang, F. Bin, Z. Teng, X. Wei, B. Dou, S. Kasipandi, Evolution behavior and active oxygen quantification of reaction mechanism on cube Cu$_2$O for CO self-sustained catalytic combustion and chemical-looping combustion, Appl. Catal. B. 310 (2022), 121296.

[49] S.L. Chen, T. Cao, Y.X. Gao, D. Li, F. Xiong, W. Huang, Probing surface structures of CeO$_2$, TiO$_2$ and Cu$_2$O nanocrystals with CO and CO$_2$ chemisorption, J. Phys. Chem. C 120 (2016) 21472–21485.

[50] Y. Zhou, A.L. Chen, J. Ning, W. Shen, Electronic and geometric structure of the copper-ceria interface on Cu/CeO$_2$ catalysts, Chin. J. Catal. 41 (2020) 928–937.

[51] F. Dong, Y. Meng, W. Han, H. Zhao, Z. Tang, Morphology effects on surface chemical properties and lattice defects of Cu/CeO$_2$ catalysts applied for low-temperature CO oxidation, Sci. Rep. 9 (2019) 12056.

[52] W.W. Wang, W.Z. Yu, P.P. Du, H. Xu, Z. Jin, R. Si, C. Ma, S. Shi, C.J. Jia, C.H. Yan, Crystal plane effect of ceria on supported copper oxide cluster catalyst for CO oxidation: Importance of metal-support interaction, ACS Catal. 7 (2017) 1313–1329.

[53] P. Bera, A.L. Cámara, A. Hornés, A. Martínez-Arias, Comparative in Situ DRIFTS-MS study of ^{12}CO- And ^{13}CO-TPR on CuO/CeO$_2$ catalyst, J. Phys. Chem. C 113 (2009) 10689–10695.

[54] A. Hornés, P. Bera, A.L. Cámara, D. Gamarra, G. Munuera, A. Martínez-Arias, CO-TPR-DRIFTS-MS in situ study of CuO/Ce$_{1-x}$Tb$_x$O$_{2-y}$ (x=0, 0.2 and 0.5) catalysts: Support effects on redox properties and CO oxidation catalysis, J. Catal. 268 (2009) 367–375.

[55] Z.H. Zhang, L.P. Fan, W.Q. Liao, F.Y. Zhao, C. Tang, J. Zhang, M. Feng, J.Q. Lu, Structure sensitivity of CuO in CO oxidation over CeO$_2$-CuO/Cu$_2$O catalysts, J. Catal. 405 (2022) 333–345.

[56] T. Andana, M. Piumetti, S. Bensaid, N. Russo, D. Fino, Heterogeneous mechanism of NO$_x$-assisted soot oxidation in the passive regeneration of a bench-scale diesel particulate filter catalyzed with nanostructured equimolar ceria-praseodymia, Appl. Catal. A Gen. 583 (2019), 117136.

[57] Y.X. Gao, Z.H. Zhang, Z.R. Li, W. Huang, Understanding morphology-dependent CuO$_x$-CeO$_2$ interactions from the very beginning, Chin. J. Catal. 41 (2020) 1006–1016.